


Noninvasive multimodal fluorescence and magnetic resonance imaging of whole-organ intervertebral discs

WUWEI REN,^{1,4} SHANGBIN CUI,^{2,3,4} MAURO ALINI,² SIBYLLE GRAD,² QUANYU ZHOU,¹  ZHEN LI,^{2,5} AND DANIEL RAZANSKY^{1,6}

¹*Institute for Biomedical Engineering and Institute of Pharmacology and Toxicology, University of Zurich and ETH Zurich, 8093 Zurich, Switzerland*

²*AO Research Institute Davos, 7270 Davos, Switzerland*

³*The First Affiliated Hospital of Sun Yat-sen University, 510080 Guangzhou, China*

⁴*equal contribution*

⁵*zhen.li@aofoundation.org*

⁶*daniel.razansky@uzh.ch*

Abstract: Low back pain (LBP) is a commonly experienced symptom posing a tremendous healthcare burden to individuals and society at large. The LBP pathology is strongly linked to degeneration of the intervertebral disc (IVD), calling for development of early-stage diagnostic tools for visualizing biomolecular changes in IVD. Multimodal measurements of fluorescence molecular tomography (FMT) and magnetic resonance imaging (MRI) were performed on IVD whole organ culture model using an in-house built FMT system and a high-field MRI scanner. The resulted multimodal images were systematically validated through epifluorescence imaging of the IVD sections at a microscopic level. Multiple image contrasts were exploited, including fluorescence distribution, anatomical map associated with T1-weighted MRI contrast, and water content related with T2 relaxation time. The developed multimodality imaging approach may thus serve as a new assessment tool for early diagnosis of IVD degeneration and longitudinal monitoring of IVD organ culture status using fluorescence markers.

© 2021 Optical Society of America under the terms of the [OSA Open Access Publishing Agreement](#)

1. Introduction

Low back pain (LBP) is a commonly encountered health problem among working-age adults with 50-80% of the population suffering from the disease during their life spans. LBP is ranked as the main cause of disability among other conditions globally [1,2]. Its prevalence and incidence generally rise with age [3,4] while adults of working age are considered the most vulnerable group susceptible to LBP. Despite its prevalence, there is little consensus regarding the LBP epidemiology [5,6]. The societal and economic costs of LBP are substantial, especially when considering both direct medical costs and indirect damages due to loss in productivity. The United States has been spending more than 100 billion dollar on LBP-related healthcare yearly [7]. The financial burden related to LBP may vary across different countries but, generally, similar relative levels of healthcare expenses are observed across the world [8–10].

To date, it is believed that degeneration of the intervertebral disc (IVD) is a major contributor to LBP [11]. The intervertebral disc contains the soft and gelatinous nucleus pulposus (NP), which is surrounded by the fibrocartilaginous annulus fibrosus (AF), and the cartilaginous endplate (EP) which connect the IVD to the adjacent vertebrae [12]. The present treatment options for LBP include pharmacological treatments, therapeutic injections with fluoroscopically guided procedures, physical modalities, psychological treatments, and spinal surgeries [5].

The mainstream diagnostic imaging methods for LBP and IVD degeneration include planar X-ray (including myelography), X-ray computed tomography (CT), and magnetic resonance

imaging (MRI). Planar X-ray, or plain radiography, provides two dimensional images with rich contrast of bone tissues and constitutes the most commonly used technique due to its relatively low cost and widespread deployment in hospitals [13]. Compared with planar X-ray, CT can provide high-resolution anatomical information in 3D, and has a well-recognized role in the diagnosis of herniated discs [14]. Nevertheless, both modalities release ionizing radiation thus elevating the health risks for patients. In contrast, MRI has the advantage of not using ionizing radiation while manifesting excellent soft tissue contrast [15,16]. Yet, MRI has higher maintenance and operational costs thus lower availability when compared with other radiological methods, especially in developing countries. Myelography is an additional LBP diagnostic method that uses a real-time form of X-ray and involves injection of contrast medium in the lumbar spine, typically followed by X-ray, CT or MRI [17].

Nevertheless, these well-established imaging techniques primarily focus on the morphological tissue changes. LBP-associated pathological evidences, such as lumbar disc herniation (LDH), can only be detected directly or indirectly at a severe stage, when significant tissue degeneration and clinical symptoms have already occurred. Finding a proper imaging tool for identification of molecular changes, especially at an early disease stage, is of high demand. It is generally believed that early diagnosis and prevention of disc degeneration is poised to significantly improve outcomes while reducing disability and associated cost [6]. Biomolecular changes are commonly taking place at the early stage of disc degeneration, such as changes in proteoglycans and collagen, major components of the IVD extracellular matrix (ECM) [18]. During the early degeneration phase, the ECM protein are cleaved into segments by matrix metalloproteinases (MMPs) and a disintegrin and metalloproteinase with thrombospondin motifs (ADAMTS). New protein structures are exposed at the cleavage sites of ECM proteins, the so called neoepitopes. Molecular imaging reflecting these biomolecular changes could make it possible to detect IVD degeneration at an early stage, e.g., via specific fluorescent probes targeting the ECM neoepitopes or proteinases [19–21]. Therefore, novel imaging approaches enabling highly sensitive and specific depiction or visualization of the biomolecular dysregulation in the ECM have the potential for early IVD degeneration diagnosis.

Fluorescence molecular tomography (FMT) is capable of visualizing 3D distribution of fluorescent probes with high sensitivity, low cost, and absence of ionizing radiation [22], thus constituting an emerging molecular imaging tool in many fields of biomedical research, such as oncology [22], brain disease [23], and drug development [24]. Typically, FMT employs near infrared (NIR) light as an illumination source and operates at penetration depth scales of several millimeters to a centimeter. Tomographic fluorescence signals are resolved by using a model-based image reconstruction algorithm, that contains a forward model for predicting the light propagation pattern in living tissue and an inversion step for recovering the fluorescence distribution iteratively [25]. In addition, FMT technology can be combined with another high-resolution structural imaging technology, such as MRI [26]. Multimodal imaging with FMT and MRI provides complementary molecular and structural information, which makes this method attractive for diagnostics in IVD degeneration, because both early-stage biomolecular and morphological changes can be recorded. Besides numerical simulation studies on FMT reconstruction of a spine sample [27], there have been no reports on the application of FMT and its multimodal strategy in the imaging of IVDs. The current study has aimed at developing a novel synergistic method for imaging IVD at the whole organ scale with FMT-MRI multimodalities. The IVD organ culture model within bioreactor has been well-established [28,29] as an ex vivo platform for preclinical testing of therapeutic treatments and diagnostics methods of IVD degeneration. We attempted multimodal MRI and FMT imaging for multi-parametric noninvasive characterization of IVD samples, and investigated various organ culture models for optimal probe delivery to facilitate FMT imaging.

2. Methods

The workflow of the study consists of three parts: 1) IVD sample preparation, 2) Noninvasive multimodal imaging, and 3) Histology and validation (Fig. 1). After injection or infiltration of fluorescent dye, the IVD samples were imaged via a raster scanning FMT and a high-field MRI scanner. Three dimensional (3D) fluorescence signal was reconstructed by FMT, and several different MRI contrast images were rendered, including a T2 relaxation map revealing the water content. Finally, epifluorescence imaging of the IVD sections were performed on all IVD samples for validation of the novel FMT-MRI imaging method.

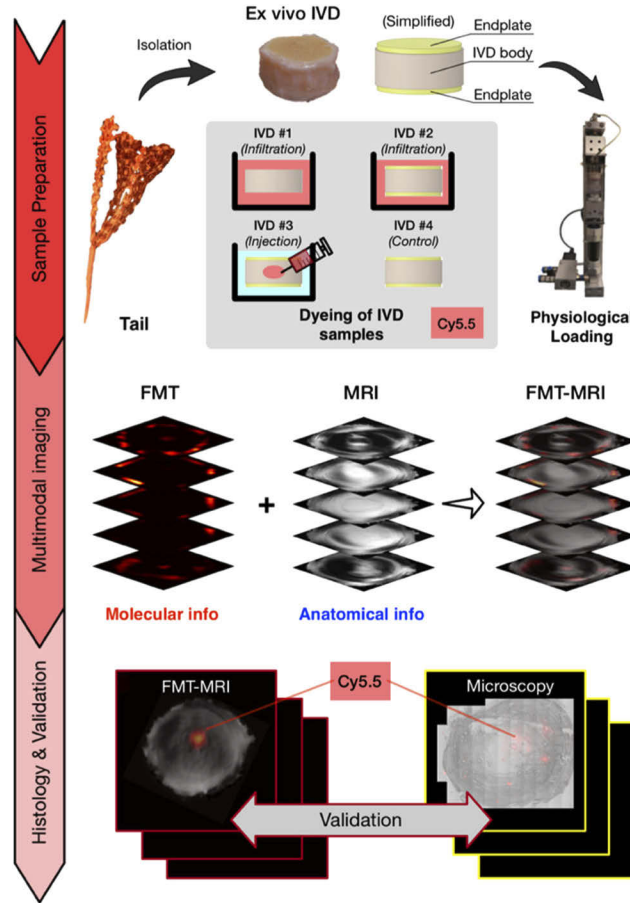


Fig. 1. The workflow of the study incorporates three parts: 1) IVD sample preparation, 2) Noninvasive multimodal imaging, and 3) Histology and validation. For sample preparation (upper panel), the IVD samples were isolated from bovine caudal spines. Different dyeing strategies were applied to IVD #1-4, followed by physiological loading. For longitudinal observation of IVD samples, a multimodal imaging paradigm was applied to render volumetric molecular information via FMT, and anatomical information via MRI (middle). Finally, the reconstructed FMT signal was validated by a histological analysis under microscopy (bottom).

2.1. Preparation of ex vivo intervertebral disc model

Caudal bovine IVDs were obtained from animals (4-10 months old) as previously described [30,31]. Briefly, after removal of the soft tissues, IVDs comprising endplates were harvested

using a band-saw. The endplates with a thickness of 1-2 mm were rinsed with Ringer solution using the Pulsavac jet-lavage system (Zimmer, Warsaw, Indiana, USA). The IVDs were further incubated in 1000 units/mL penicillin, 1000 µg/mL streptomycin in phosphate buffered saline (PBS) solution for 10 min. Afterwards, the cleaned discs were transferred to 6 well-plates and kept in an incubator at 37°C, 85% humidity and 5% CO₂ until the next day. The culture medium was composed of Dulbecco's modified Eagle medium (DMEM) containing 4.5 g/L glucose and supplied with 2% fetal calf serum, 1% ITS+ Premix (Discovery Labware, Inc., Bedford, USA), 50 µg/mL ascorbate-2-phosphate (Sigma-Aldrich, St. Louis, USA), non-essential amino acids, 100 units/mL penicillin, 100 µg/mL streptomycin (all except for mentioned, Gibco, Basel, Switzerland) and 0.1% Primocin (Invitrogen, San Diego, CA, USA).

Four IVD samples were used in the study (diameter, 17.00 ± 2.56 mm; height, 11.78 ± 1.07 mm). In order to compare different modes of contrast agent uptake, a solution containing fluorescent dye was either infiltrated or injected into IVD samples. To understand the contribution of the appearance of endplates toward the fluorophore absorption, the bony endplate of IVD organ culture model was either preserved or removed by the high speed drill. The first and second samples, denoted as IVD #1 (without bony endplate) and #2 (with bony endplate), were immersed in culture medium containing Cyanine 5.5 (Cy5.5, NHS ester, abcam, USA, 100 µL, 10^{-4} mol/L of Cy5.5 solution in 5 mL culture medium). For IVD #3 (with bony endplate), 100 µL, 10^{-4} mol/L of Cy5.5 solution was injected into the central part of the NP through the AF with a 30G insulin needle (Braun, Melsungen, GE). IVD #4 was used as a negative control. Cy5.5 was applied as the fluorescent probe with peak absorption and emission at 680 nm and 720 nm wavelengths, respectively.

Physiological loading was applied on the IVDs within a custom designed bioreactor at 0.02-0.2 MPa, 0.2 Hz, 2 hours per day to mimic diffusion of the fluorescent dye under *in vivo* loading condition [12]. The bioreactor was maintained in an incubator at 37°C, 85% humidity and 5% CO₂. After loading, the IVDs were cultured in 6-well plates for overnight free swelling recovery. The same medium of the IVD samples was used, both during loading and free swelling. IVD #1-3 received physiological loading for 2 days before MRI and FMT imaging were performed.

2.2. Magnetic resonance imaging on IVD samples

MRI measurements were carried out with a high-field scanner (BioSpec 94/30, Bruker BioSpin, Ettlingen, Germany) featuring a 9.4T magnet, 30-cm diameter clear bore, and a high performance B-GA 12S gradient system [32]. Before data acquisition, each IVD sample was wrapped with a polyethylene foil, and loaded onto a phased-array CryoProbe for signal reception combined with a whole-body bird cage resonator for radiofrequency (RF) transmission. High-resolution anatomical MRI stacks with T1-weighted contrast were acquired using a gradient echo sequence (configuration: field of view (FOV) = 30×30 mm², dimension of reconstructed matrix = $300 \times 300 \times 13$, Echo time (TE) = 4 ms, repetition time (TR) = 250 ms, flip angle (FA) = 30 degree, slice thickness = 1 mm).

Additionally, in order to quantify the water content of the IVDs, mapping of the T2 relaxation parameter was performed at the central cross section of the IVD sample. The section was recorded using a multislice multi-spin-echo pulse sequence containing 25 different TE values from 9 ms up to 225 ms with 9 ms steps. Other configuration parameters are as following: FOV = 30×30 mm², dimension of reconstructed matrix = 300×300 , TR = 2000 ms, FA = 30 degree, slice thickness = 3 mm. The T1-weighted image reconstruction and recovery of the T2 maps were performed with ParaVision 6.0 (Bruker BioSpin, Ettlingen, Germany).

2.3. Fluorescence molecular tomography on IVD samples

FMT data acquisition was performed with IVD samples (#1-4) using an in-house-built system, as previously reported [33,34]. Briefly, we used a continuous wave (CW) laser at 670 nm

wavelength (B&W Tek, Newark, USA). The laser beam was directed by a galvanometric driven mirror (Scancube, ScanLab, Puchheim, Germany) and raster scanning was implemented in a point-by-point manner forming a 7×7 illumination grid. The IVD samples were loaded on a customized support containing a transparent window allowing a transmission-mode data acquisition, i.e., illumination and detection were located on the opposite sides of the sample. Both raw images at the excitation and fluorescence wavelengths were acquired by adjusting the filter wheel to wavelengths of 670 nm and 700 nm, respectively. A 1024×1024 16-bit CCD camera (ANDOR, Belfast, Northern Ireland) was operated at -80°C to reduce the dark noise in the images (Fig. 2, top).

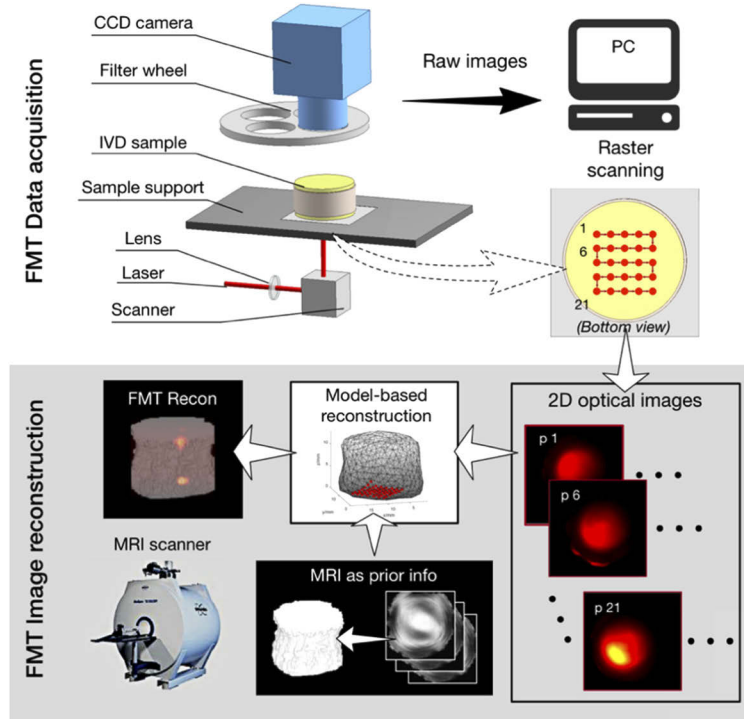


Fig. 2. FMT data acquisition (upper panel) and image reconstruction (lower panel). During data acquisition, the bottom of the IVD sample was illuminated by a laser beam with a raster scanning manner as illustrated on the right middle. Raw images acquired at both excitation and emission wavelengths were transferred to a computer. An MRI-assist model-based image reconstruction algorithm was adopted to recover the three-dimensional fluorophore distribution, using the planar images obtained at different positions of illumination.

After data acquisition, the raw images from the CCD camera were transferred into a customized software platform (STIFT, [25]) for model-based FMT image reconstruction (Fig. 2, bottom). The STIFT platform features a modular design that incorporates multiple functions during FMT data processing including image registration, meshing, forward modeling and inversion [25]. The MRI images of each IVD sample were segmented and meshed into tetrahedral elements to be used as prior information for the FMT inversion (Fig. 2, bottom). Diffuse light propagation was modeled via a finite element method (FEM) by assigning known optical properties to the meshed volume. For simplicity, we assumed a homogeneous object with reduced scattering coefficient $\mu'_s = 0.5 \text{ mm}^{-1}$, absorption coefficient $\mu_a = 0.0008 \text{ mm}^{-1}$, and refractive index $n = 1.4$, according to previously reported values [27]. A quasi-Newton method was applied for the consequent inversion step with regularization parameter $\tau = 5 \times 10^{-3}$ and 100 maximum

number of iterations. Previously we have demonstrated the reliability of the homebuilt FMT setup and reconstruction algorithm [25,33]. A tissue-mimicking cylindrical phantom (radius, 30 mm; height, 20 mm) with optical heterogeneity and deeply seated fluorophore inclusion (Cy5.5 solution) was imaged using an excitation light beam at 670 nm and detection of the emitted fluorescence at 700 nm. Subsequently, a point-shaped fluorophore inclusion at the depth of 11.5 mm was accurately reconstructed [33]. All the image reconstruction procedures were performed in MATLAB (R2019a, MathWorks Inc., Natick, MA, US) on a desktop computer (Intel core i7, 2.60 GHz; RAM, 8.00 GB).

2.4. *Histological studies via microscopic imaging*

After multimodal imaging with MRI and FMT, all IVD samples were snap-frozen and immersed in a cryo-embedding compound (Tissue-Tek, O.C.T.TM, Sismex, Horgen, Switzerland). Transverse sections of IVDs were made at a thickness of 10 μm by a cryostat. The transverse sections were imaged under an upright optical microscope (EVOS FLoid Auto 2, Thermo Fisher, USA). Transmission-mode illumination was applied by setting the excitation wavelength to 673 nm and fluorescence wavelength to 707 nm to match the spectrum of Cy5.5 dye. In addition to the fluorescence image, a white-light image was also taken for each section to capture structural information from the IVDs. The raw data of microscopic images feature constant parameters with image resolution of 24270×24270 dpi.

3. Results

3.1. *MRI T1-weighted and T2 mapping images*

High-resolution structural images were achieved by T1-weighted images for all IVDs (Fig. 5). Among 13 slices acquired with T1-weighted contrast, 5 representative slices are shown here (Fig. 5(b)-(e)). The fibrous rings in the periphery of IVDs were clearly resolved, whereas the central parts of IVDs manifested a homogenous texture representative of NP. The structural information given by T1-weighted images served as a reference in the T2 mapping and fluorescence images.

To quantitatively evaluate the water content of IVDs, the mapping of T2 relaxation time was subsequently performed. The T2 mapping images were calculated from a series of raw T2-weighted images by continuously changing the TE value, an important parameter in the MRI acquisition configuration (Fig. 3(a)-(d)). For each IVD sample, a central slice with T2 mapping contrast was obtained (Fig. 3(e)-(h)). Compared with the structural image by T1-weighted contrast (Fig. 5(b)), T2 mapping images exhibited lower number of ring-shaped patterns, but rather a significantly higher intensity in the central part of the IVD, corresponding to the high water content in the NP. To remove the artifacts, a threshold of 140 ms was applied to all IVDs. T2 relaxation time profiles along x- and y-axes were plotted at the central (150,150) point in a pixel-based coordinate (Fig. 4(a),(b)). The mean values and standard deviations of x-axis profiles were 80.29 ± 35.27 , 70.24 ± 29.34 , 68.51 ± 29.51 , 68.59 ± 26.53 for IVD #1-4, respectively, whereas the values of y-axis profiles were 81.46 ± 33.40 , 77.22 ± 39.34 , 67.27 ± 35.05 , 91.16 ± 15.62 , in good agreement with previous findings [35]. We have also identified different regions of interest (ROIs) of NP and AF based on the anatomical MRI images, and calculated mean values and standard deviation of T2 relaxation time based on the ROIs. As shown in Fig. 4(c), the mean value of NP ranges between 68.12 and 77.89, whereas the corresponding range for AF was 20.3 - 33.27, indicating the water content in AF is approximately 60% less than that in NP.

3.2. *FMT reconstruction with MRI as prior information*

The 3D distribution of fluorescent probe (Cy5.5 in this case) was obtained by FMT noninvasively. The T1-weighted MRI images achieved in the previous section serve a twofold function. Firstly,

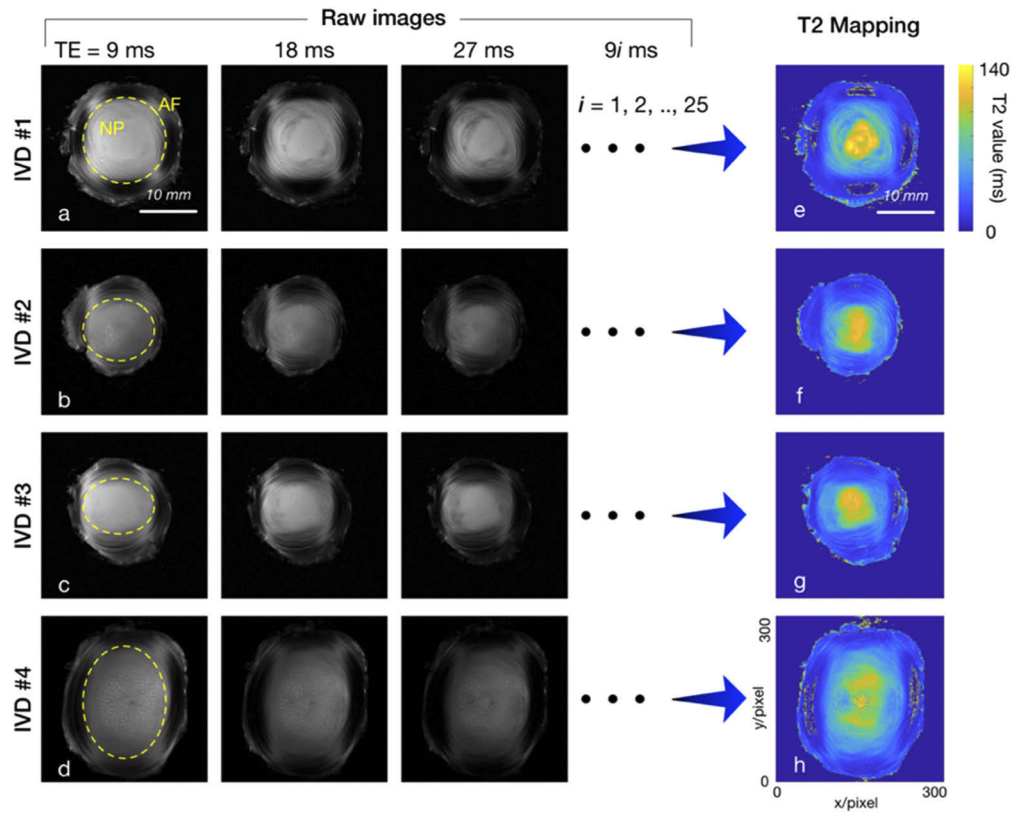


Fig. 3. Raw T2-weighted MRI images of four IVDs are displayed on the left with a series of different TE values (a-d). Such series of T2-weighted images can yield mapping of quantitative T2 relaxation values (e-h), contributing to the evaluation of the water content inside samples. ROI inside the dashed yellow circle indicates the part of NP, while the outside represents AF. All T2 mapping images were with a threshold of 140 ms.

the MRI images can be used as a priori information for the FMT reconstruction algorithm. The MRI slices were segmented and meshed to generate a mesh containing tetrahedral elements and assigned optical properties. Secondly, the reconstructed fluorophore can be overlaid with the MRI images, leading to a better localization of the fluorescence signal. Herein, we utilized MRI information to attain FMT reconstructions for IVD #1-3. The FMT reconstruction for IVD #4 was not applicable, as the fluorescence signal was negligible in this case. All reconstruction results of FMT were interpolated into the same matrix size as the MRI stacks, i.e., $300 \times 300 \times 13$, for convenience of visualization and data analysis. Each slice of the FMT reconstruction (Fig. 5(a)) was overlaid with the corresponding MRI images, resulting in combined FMT-MRI images for IVD #1-3 (Fig. 5(c)-(e)). For IVD #1 and #2, the majority of fluorescence signal was observed in the periphery of IVD samples, namely the AF part, whereas for IVD #3, the fluorescence signal was more concentrated in the NP location with a big droplet (extending about 2 mm) close to the upper surface and a small one close to the bottom surface. No obvious fluorescence signal was found in AF regions. Figure 6 shows the maximum intensity projection (MIP) of the volumetric FMT data and the 3D iso-surface of segmented MRI data. The overlaid FMT-MRI 3D visualization allows for a comprehensive understanding of where exactly the fluorophore is distributed within the IVD samples.

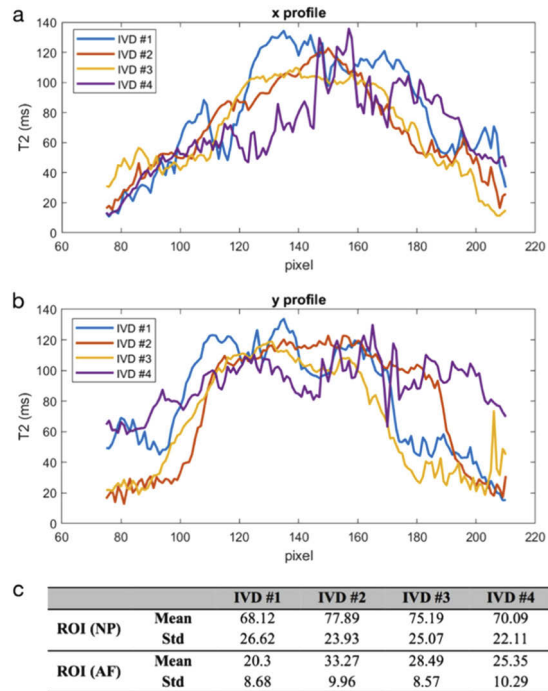


Fig. 4. (a) and (b) show the profile drawing along x- and y- axes of T2 mapping images centered around (150,150) point. All profiles have high T2 values at the center of IVDs, indicating a high water composition. The table of ROI analysis (c) shows a similar result.

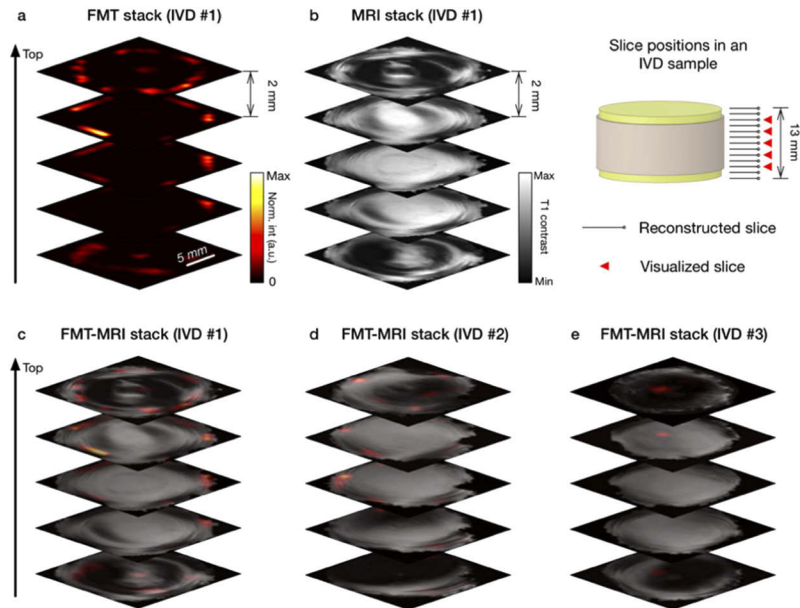


Fig. 5. A volumetric stack of the reconstructed FMT (a) and MRI (b) images is displayed with a step size of 2 mm. (c)-(e) The overlaid FMT and MRI image stacks for IVD #1-#3. For all IVD samples, 13 slices in total were reconstructed with FMT and 5 representative slices selected for visualization (marked red).

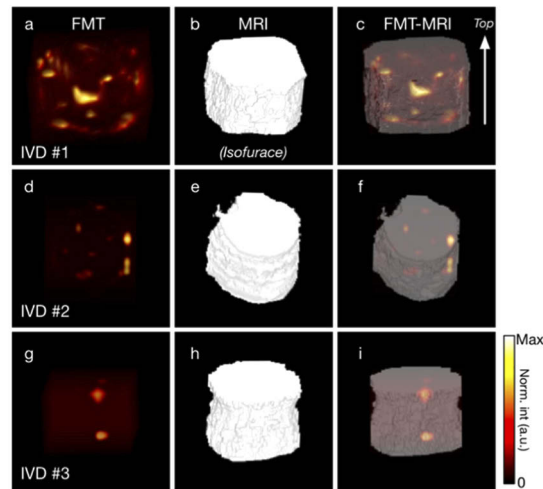


Fig. 6. The left column shows 3D MIP visualization of the volumetric FMT data (a,d,g). The middle column shows the segmented iso-surface of the MRI data (b,e,h). Both FMT and MRI images were registered and overlaid in 3D (c,f,i).

3.3. Validation via microscopic images

Histological studies were performed to compare and validate the tomographic multimodal FMT-MRI reconstructions of intact samples with their transverse cross sections under microscopy. We overlaid both microscopic images filtered with the fluorescence emission wavelength and without any filter (also called white-light images). The former should generally correspond to the information obtain via FMT, while the latter to structural images rendered with MRI. As shown in Fig. 7, for the slices at a 7 mm depth (i.e. distance from the top cartilage endplate) high intensity of fluorescence signals was found in the AF area in both multimodal FMT and microscopy images for IVD #1 and #2. Additionally, for the slice at a depth of 3mm in IVD #3, both FMT and microscopy displayed a fluorescence signal concentrated in the NP part. At a

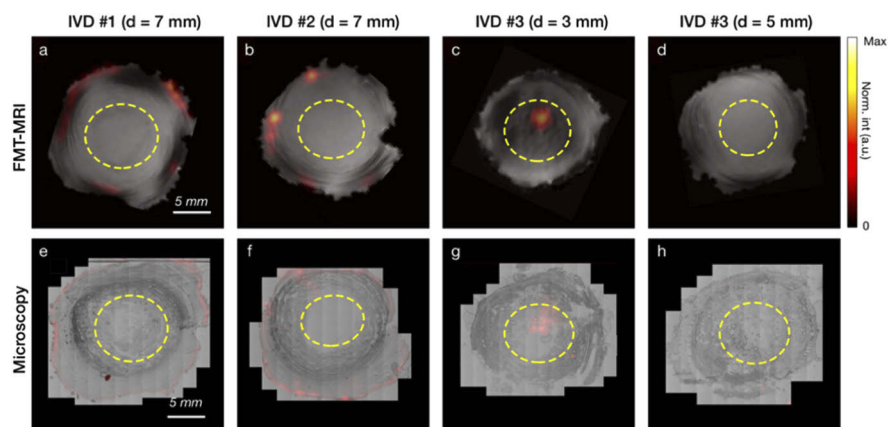


Fig. 7. Validation of the FMT-rendered fluorescence reconstructions via histological microscopy studies. The upper row shows overlaid FMT-MRI images for different IVD samples with the depth indicated. The lower row shows the corresponding microscopic images. The yellow dashed circles separate the ROIs for NP and AF parts.

depth of 5 mm in the same IVD, negligible signal was found with both modalities. A further quantitative analysis was performed by calculating the average value of signal intensity in the ROIs of NP and AF. Figure 8 shows that the multimodal FMT-MRI yielded results in good agreement with microscopic histological studies. It was noticeable that FMT reconstruction in each slice had lower resolution, typically in the 1-2 mm range, when compared with transverse sections obtained from 2D high-resolution microscope. However, the noninvasive FMT provided a similar spatial pattern of fluorescence that correlated well with microscopic images.

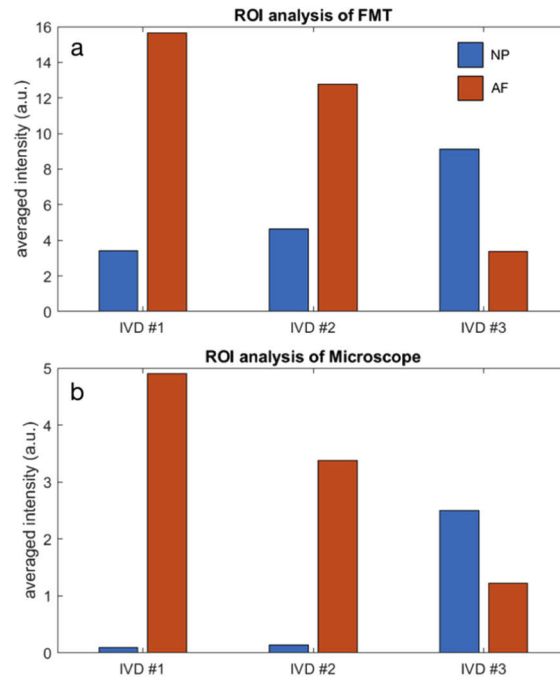


Fig. 8. Quantitative analysis based on two ROIs in both FMT (a) and microscopic (b) images of the IVD. The average values of fluorescence signal in NP and AF agree well between the two optical imaging modalities.

4. Discussion

LBP is a commonly encountered symptom that imposes a heavy burden on individual health and society at large. Traditional diagnostic tools such as X-ray, CT, and MRI are only capable of detecting the morphological changes in IVD degeneration, when significant damage and clinical symptoms have already developed. Hence it is imperative to explore novel imaging approaches enabling sensitive and specific visualization and assessment of biomolecular changes underlying IVD degeneration at an early stage. FMT is capable of retrieving the 3D bio-distribution of fluorescent molecular markers noninvasively [22], thus offering higher molecular sensitivity compared to other traditional modalities, such as CT or MRI [24]. One key aspect of FMT is the use of NIR fluorescence probes, which have been shown to be the most effective for deep in vivo imaging. In the NIR spectral range, the attenuation of living tissue is minimal, allowing the use of sufficient laser power for fluorescence excitation and detection without causing tissue damage under prolonged illumination.

To this end, the use of FMT for bone imaging has been limited to small animals [36]. Herein, we described the first attempt towards FMT of the ex vivo bovine IVD organ culture model in its entirety (~1-2 cm thickness). More precisely, we aim at a longitudinal imaging solution

that serves the orthopedic research to investigate the role of IVD degeneration in LBP. An in-house built FMT system [34] was applied to image four IVDs including three samples bearing fluorescent dye and one without, as a negative control. FMT could clearly discern the different concentration of fluorescent dye in AF and NP (Fig. 5). Stronger fluorescence was observed in outer region of the AF than in the NP in IVD #1 and #2, whereas the signal in IVD #3 was mainly concentrated in the center of the NP. These results are ascribed to the different ways the dye was introduced into the IVDs: the first two samples were immersed in culture medium containing the dye, whilst the third sample was dyed by injection into the NP through the AF. By comparing Fig. 6(a) and Fig. 6(d), a stronger fluorescence signal is found in the peripheral AF region in IVD #1 versus IVD #2. This can be explained by the removal of bony endplates in IVD #1, making the surrounding Cy5.5 more accessible through the cartilage endplate. The tomographic performance of FMT was further validated through histological studies with microscopy. Although the spatial resolutions were different for the two modalities, they share similarities in the fluorescence pattern retrieved (Figs. 7 and 8).

Furthermore, we applied a multimodal FMT method with additional measurement in a high-field MRI scanner (9.4T). Two types of MRI contrast images were acquired. The T1-weighted MRI images attained a clear anatomical reference that was used to enhance FMT image reconstruction and localization of the fluorescence biodistribution (Fig. 5). In addition, the T2 relaxation time images reliably represented the water content in the IVD. In this study, we found the water content in the AF amounted to 30-40% of that in the NP, which correlated well with the literature [35]. The quantitative analysis of T2 mapping is known for its capability to assess different levels of IVD degeneration [37]. In both types of images, the high-field preclinical MRI scanner achieved superior spatial resolution with more structural details of IVDs revealed (e.g., fibrous rings) as compared with the images acquired with clinical scanners (1.5T-3T) [35,37].

The current study established a multimodal FMT-MRI imaging protocol for longitudinal investigation of the IVD biological structure at the whole organ level. For the demonstration purposes, a commonly used non-specific Cy5.5 fluorescent dye was used. However, new types of fluorescent contrast agents that indicate early-stage biomolecular changes in IVD could be developed and utilized in order to form a complete diagnostic toolbox with the proposed imaging technology. Some promising molecular targets for the fluorescence labelling include neoepitopes, MMPs, and ADAMTS, that are crucial in the IVD ECM turnover [38,39,40]. Our previous work has established early degeneration IVD organ culture models using detrimental mechanical loading protocols [28,29]. In future studies, these models will be used to further unveil the potential of the FMT-MRI imaging system in combination with fluorescence probes targeting pathological molecular alterations for diagnosis of an early IVD degeneration. In clinical case, the probe could be delivered into the vertebrae body through transpedicular approach and diffuse into the IVD through the cartilage endplate [41]. Alternatively, the probe could be injected into the IVD through the annulus fibrosus of adjacent IVD segment during surgery of trauma injured IVD. Penetration depth of the fluorescent signal may be a limiting factor for application of this method clinically. However, it is also to be noted that the spinal IVDs are generally located in proximity to the skin surface. Further simulation study is warranted using MRI data of LBP patients to validate the clinical feasibility of the suggested methodology [42,43]. When considering clinical translation aspects, reflectance mode FMT is preferred as the illumination and detection are performed on the same side of the object. However, transmission-mode FMT is known to achieve better spatial resolution in deep tissues [44]. In the current feasibility study employing *ex vivo* IVD samples, transmission-mode configuration was applied to render a more accurate maps of fluorophore distribution within the sample. Yet, a more comprehensive comparison between the two imaging modes for IVD observations should be aimed in future studies. In addition, introduction of advanced reconstruction algorithms with non-negativity constraints and the emerging application of NIR-II window (1000-1700 nm) may further improve the spatial

resolution and penetration depth of FMT [45–47]. Beyond the FMT modality, an emerging optoacoustic imaging methods and their multimodal combinations may serve as an alternative for anatomical, functional and molecular imaging of IVDs with superb spatial resolution, contrast and specificity [48–50].

5. Conclusion

We have established a multimodal imaging protocol for investigating its potential for early diagnostics in IVD degeneration. Sequential FMT and MRI measurements were performed on the ex vivo bovine IVD model using an in-house built FMT system and a high-field preclinical MRI scanner. Tomographic fluorescence images were reconstructed noninvasively, overlaid with an anatomical reference provided by T1-weighted MRI images. Additionally, T2 relaxation time mapping was also achieved to quantify the water concentration in IVDs. The results were systematically validated through microscopic histological studies. The FMT-MRI multimodal imaging method can serve as a powerful tool in the research quest to better understand the etiology of IVD degeneration.

Funding. Swiss National Science Foundation (178262); AO Foundation; AO Spine International.

Acknowledgments. We thank Dr. Mark-Aurel Augath (ETH Zurich) for the guidance in MRI measurements.

Disclosures. There is no conflict of interest.

Data availability. Data underlying the results presented in this paper are not publicly available at this time but may be obtained from the authors upon reasonable request.

References

1. L. J. Jeffries, S. F. Milanese, and K. A. Grimmer-Somers, "Epidemiology of adolescent spinal pain: a systematic overview of the research literature," *Spine* **32**(23), 2630–2637 (2007).
2. D. I. Rubin, "Epidemiology and risk factors for spine pain," *Neurol. Clin.* **25**(2), 353–371 (2007).
3. I. M. B. de Souza, T. F. Sakaguchi, S. L. K. Yuan, L. A. Matsutani, A. S. do Espirito-Santo, C. A. B. Pereira, and A. P. Marques, "Prevalence of low back pain in the elderly population: a systematic review," *Clinics* **74**, e789 (2019).
4. D. Hoy, L. March, P. Brooks, A. Woolf, F. Blyth, T. Vos, and R. Buchbinder, "Measuring the global burden of low back pain," *Best Pract. Res. Clin. Rheumatol.* **24**(2), 155–165 (2010).
5. R. D. Meucci, A. G. Fassa, and N. M. Faria, "Prevalence of chronic low back pain: systematic review," *Rev. Saude Publica* **49**(0), 1 (2015).
6. F. Fatoye, T. Gebrye, and I. Odeyemi, "Real-world incidence and prevalence of low back pain using routinely collected data," *Rheumatol. Int.* **39**(4), 619–626 (2019).
7. J. N. Katz, "Lumbar disc disorders and low-back pain: socioeconomic factors and consequences," *J. Bone Jt. Surg., Am.* **88**(suppl_2), 21–24 (2006).
8. H. Liedgens, M. Obradovic, J. De Courcy, T. Holbrook, and R. Jakubanis, "A burden of illness study for neuropathic pain in Europe," *CEOR* **8**, 113–126 (2016).
9. C. J. Itz, B. L. Ramaekers, M. van Kleef, and C. D. Dirksen, "Medical specialists care and hospital costs for low back pain in the Netherlands," *Eur. J. Pain.* **21**(4), 705–715 (2017).
10. B. F. Walker, R. Muller, and W. D. Grant, "Low back pain in Australian adults: the economic burden," *Asia Pac. J. Public Health* **15**(2), 79–87 (2003).
11. A. J. Freemont, "The cellular pathobiology of the degenerate intervertebral disc and discogenic back pain," *Rheumatology* **48**(1), 5–10 (2008).
12. G. Lang, Y. Liu, J. Geries, Z. Zhou, D. Kubosch, N. Sudkamp, R. G. Richards, M. Alini, S. Grad, and Z. Li, "An intervertebral disc whole organ culture system to investigate proinflammatory and degenerative disc disease condition," *J. Tissue Eng. Regener. Med.* **12**(4), e2051–e2061 (2018).
13. D. Kendrick, K. Fielding, E. Bentley, R. Kerslake, P. Miller, and M. Pringle, "Radiography of the lumbar spine in primary care patients with low back pain: randomised controlled trial," *BMJ* **322**(7283), 400–405 (2001).
14. J. D. Lurie, "What diagnostic tests are useful for low back pain?" *Best Pract. Res. Clin. Rheumatol.* **19**(4), 557–575 (2005).
15. J. G. Jarvik and R. A. Deyo, "Diagnostic evaluation of low back pain with emphasis on imaging," *Ann. Intern. Med.* **137**(7), 586–597 (2002).
16. M. Wassenaar, R. M. van Rijn, M. W. van Tulder, A. P. Verhagen, D. A. van der Windt, B. W. Koes, M. R. de Boer, A. Z. Ginai, and R. W. Ostelo, "Magnetic resonance imaging for diagnosing lumbar spinal pathology in adult patients with low back pain or sciatica: a diagnostic systematic review," *Ann. Intern. Med.* **21**(2), 220–227 (2012).

17. T. Matsumoto, S. Imagama, H. Inoue, T. Aoki, N. Ishiguro, and Y. Osawa, "Outpatient myelography: a prospective trial comparing complications after myelography between outpatients and inpatients in Japan," *Asian Spine J.* **9**(6), 928–934 (2015).
18. J. Antoniou, T. Steffen, F. Nelson, N. Winterbottom, A. P. Hollander, R. A. Poole, M. Aebi, and M. Alini, "The human lumbar intervertebral disc: evidence for changes in the biosynthesis and denaturation of the extracellular matrix with growth, maturation, ageing, and degeneration," *J. Clin. Invest.* **98**(4), 996–1003 (1996).
19. M. Rudin, *Molecular Imaging: Basic Principles and Applications in Biomedical Research* (Imperial College Press, 2012).
20. W. T. Chen, U. Mahmood, R. Weissleder, and C. H. Tung, "Arthritis imaging using a near-infrared fluorescence folate-targeted probe," *Arthritis Res. Ther.* **7**(2), R310–R317 (2005).
21. W. Yi, H. Zhou, A. Li, Y. Yuan, Y. Guo, P. Li, B. Qi, Y. Xiao, A. Yu, and X. Hu, "A NIR-II fluorescent probe for articular cartilage degeneration imaging and osteoarthritis detection," *Biomater. Sci.* **7**(3), 1043–1051 (2019).
22. V. Ntziachristos, C. H. Tung, C. Bremer, and R. Weissleder, "Fluorescence molecular tomography resolves protease activity in vivo," *Nat. Med.* **8**(7), 757–761 (2002).
23. D. Hyde, R. de Kleine, S. A. MacLaurin, E. Miller, D. H. Brooks, T. Krucker, and V. Ntziachristos, "Hybrid FMT-CT imaging of amyloid-beta plaques in a murine Alzheimer's disease model," *NeuroImage* **44**(4), 1304–1311 (2009).
24. F. Stuker, J. Ripoll, and M. Rudin, "Fluorescence molecular tomography: principles and potential for pharmaceutical research," *Pharmaceutics* **3**(2), 229–274 (2011).
25. W. Ren, H. Isler, M. Wolf, J. Ripoll, and M. Rudin, "Smart toolkit for fluorescence tomography: simulation, reconstruction, and validation," *IEEE Trans. Biomed. Eng.* **67**(1), 16–26 (2020).
26. W. Ren, A. Elmer, D. Buehlmann, M.-A. Augath, D. Vats, J. Ripoll, and M. Rudin, "Dynamic measurement of tumor vascular permeability and perfusion using a hybrid system for simultaneous magnetic resonance and fluorescence imaging," *Mol. Imaging. Biol.* **18**(2), 191–200 (2016).
27. M. Pimpalkhare, J. Chen, V. Venugopal, and X. Intes, "Ex vivo fluorescence molecular tomography of the spine," *Int. J. Biomed. Imaging* **2012**, 1–11 (2012).
28. J. J. Pfannkuche, W. Guo, S. Cui, J. Ma, G. Lang, M. Peroglio, R. G. Richards, M. Alini, S. Grad, and Z. Li, "Intervertebral disc organ culture for the investigation of disc pathology and regeneration - benefits, limitations, and future directions of bioreactors," *Connect. Tissue Res.* **61**(3–4), 304–321 (2020).
29. Z. Zhou, S. Cui, J. Du, R. G. Richards, M. Alini, S. Grad, and Z. Li, "One strike loading organ culture model to investigate the post-traumatic disc degenerative condition," *J. Orthop. Translat.* **26**, 141–150 (2021).
30. Z. Li, P. Lezuo, G. Pattappa, E. Collin, M. Alini, S. Grad, and M. Peroglio, "Development of an ex vivo cavity model to study repair strategies in loaded intervertebral discs," *Eur. Spine J.* **25**(9), 2898–2908 (2016).
31. Z. Li, Y. Gehlen, F. Heizmann, S. Grad, M. Alini, R. G. Richards, D. Kubosch, N. Sudkamp, K. Izadpanah, E. J. Kubosch, and G. Lang, "Preclinical ex-vivo testing of anti-inflammatory drugs in a bovine intervertebral degenerative disc model," *Front. Bioeng. Biotechnol.* **8**, 583 (2020).
32. Bruker, "Bruker MRI scanner" (2020), retrieved Sep, 2020, <https://www.bruker.com/>.
33. W. Ren, J. Jiang, A. D. Costanzo Mata, A. Kalyanov, J. Ripoll, S. Lindner, E. Charbon, C. Zhang, M. Rudin, and M. Wolf, "Multimodal imaging combining time-domain near-infrared optical tomography and continuous-wave fluorescence molecular tomography," *Opt. Express* **28**(7), 9860–9874 (2020).
34. F. Stuker, "Hybrid imaging: combining fluorescence molecular tomography with magnetic resonance imaging," (ETH Zurich, 2011).
35. S. E. Detiger, R. M. Holewijn, R. J. Hoogendoorn, B. J. van Royen, M. N. Helder, F. H. Berger, J. P. Kuijter, and T. H. Smit, "MRI T2* mapping correlates with biochemistry and histology in intervertebral disc degeneration in a large animal model," *Eur. Spine J.* **24**(9), 1935–1943 (2015).
36. A. Zaheer, R. E. Lenkinski, A. Mahmood, A. G. Jones, L. C. Cantley, and J. V. Frangioni, "In vivo near-infrared fluorescence imaging of osteoblastic activity," *Nat. Biotechnol.* **19**(12), 1148–1154 (2001).
37. S. Hoppe, S. Quirbach, T. C. Mamsch, F. G. Krause, S. Werlen, and L. M. Benneker, "Axial T2* mapping in intervertebral discs: a new technique for assessment of intervertebral disc degeneration," *Eur. Radiol.* **22**(9), 2013–2019 (2012).
38. H. Y. Yuan, Y. Tang, Y. X. Liang, L. Lei, G. B. Xiao, S. Wang, and Z. L. Xia, "Matrix metalloproteinase-3 and vitamin d receptor genetic polymorphisms, and their interactions with occupational exposure in lumbar disc degeneration," *J. Occup. Health* **52**(1), 23–30 (2010).
39. S. Ricard-Blum, "The collagen family," *Cold Spring Harbor Perspect. Biol.* **3**(1), a004978 (2011).
40. S. Rajasekaran, R. M. Kanna, N. Senthil, M. Raveendran, V. Ranjani, K. M. Cheung, D. Chan, P. Y. Kao, A. Yee, and A. P. Shetty, "Genetic susceptibility of lumbar degenerative disc disease in young Indian adults," *Eur. Spine J.* **24**(9), 1969–1975 (2015).
41. G. Vadala, F. Russo, G. Pattappa, D. Schiuma, M. Peroglio, L. M. Benneker, S. Grad, M. Alini, and V. Denaro, "The transpedicular approach as an alternative route for intervertebral disc regeneration," *Spine* **38**(6), E319–E324 (2013).
42. W. Ren, A. Elmer, M.-A. Augath, and M. Rudin, "FEM-based simulation of a fluorescence tomography experiment using anatomical MR images," *Proc. SPIE* **9788**, 978828 (2016).
43. V. Ntziachristos, A. G. Yodh, M. Schnall, and B. Chance, "Concurrent MRI and diffuse optical tomography of breast after indocyanine green enhancement," *Proc. Natl. Acad. Sci. U. S. A.* **97**(6), 2767–2772 (2000).

44. J. P. Culver, V. Ntziachristos, M. J. Holboke, and A. G. Yodh, "Optimization of optode arrangements for diffuse optical tomography: a singular-value analysis," *Opt. Lett.* **26**(10), 701–703 (2001).
45. M. Cai, Z. Zhang, X. Shi, Z. Hu, and J. Tian, "NIR-II/NIR-I fluorescence molecular tomography of heterogeneous mice based on Gaussian weighted neighborhood fused Lasso method," *IEEE Trans. Med. Imaging* **39**(6), 2213–2222 (2020).
46. G. Hongbo, H. Xiaowei, L. Muhan, Z. Zeyu, H. Zhenhua, and T. Jie, "Weight multispectral reconstruction strategy for enhanced reconstruction accuracy and stability with Cerenkov luminescence tomography," *IEEE Trans. Med. Imaging* **36**(6), 1337–1346 (2017).
47. M. Cai, Z. Zhang, X. Shi, J. Yang, Z. Hu, and J. Tian, "Non-negative iterative convex refinement approach for accurate and robust reconstruction in cerenkov luminescence tomography," *IEEE Trans. Med. Imaging* **39**(10), 3207–3217 (2020).
48. W. Ren, X. L. Dean-Ben, M. A. Augath, and D. Razansky, "Development of concurrent magnetic resonance imaging and volumetric optoacoustic tomography: A phantom feasibility study," *J. Biophotonics* **14**, e202000293 (2021).
49. W. Ren, H. Skulason, F. Schlegel, M. Rudin, J. Klohs, and R. Ni, "Automated registration of magnetic resonance imaging and optoacoustic tomography data for experimental studies," *Neurophotonics* **6**(2), 025001 (2019).
50. W. Ren, H. Skulason, F. Schlegel, M. Rudin, J. Klohs, and R. Ni, "Automated registration for optoacoustic tomography and MRI," in *Biophotonics Congress: Optics in the Life Sciences*, (OSA, 2019).